RAA 2021 Vol. **21** No. **2**, 26(11pp) doi: 10.1088/1674-4527/21/2/26

http://www.raa-journal.org *http://iopscience.iop.org/raa*

***R**esearch in*
***A**stronomy and*
***A**strophysics*

Collapsing index: a new method to identify star-forming cores based on ALMA images

Nan-Nan Yue[1,2], Yang Gao[3], Di Li[1,2,4] and Liu-Bin Pan[3]

[1] National Astronomical Observatories, Chinese Academy of Sciences, Beijing 100101, China; *gaoyang25@mail.sysu.edu.cn, dili@nao.cas.cn*
[2] University of Chinese Academy of Sciences, Beijing 100049, China
[3] School of Physics and Astronomy, Sun Yat-Sen University, Zhuhai 519082, China
[4] NAOC-UKZN Computational Astrophysics Centre, University of KwaZulu-Natal, Durban 4000, South Africa

Received 2020 May 12; accepted 2020 July 19

Abstract Stars form through the gravitational collapse of molecular cloud cores. Before collapsing, the cores are supported by thermal pressure and turbulent motions. A question of critical importance for the understanding of star formation is how to observationally discern whether a core has already initiated gravitational collapse or is still in hydrostatic balance. The canonical method to identify gravitational collapse is based on the observed radial density profile, which would change from Bonnor-Ebert type toward power laws as the core collapses. In practice, due to the projection effect, the resolution limit and other caveats, it has been difficult to directly reveal the dynamical status of cores, particularly in massive star forming regions. We here propose a novel, straightforward diagnostic, namely, the collapsing index (CI), which can be modeled and calculated based on the radial profile of the line width of dense gas. A meaningful measurement of CI requires spatially and spectrally resolved images of optically thin and chemically stable dense gas tracers. ALMA observations are making such data sets increasingly available for massive star forming regions. Applying our method to one of the deepest dense-gas spectral images ever taken toward such a region, namely, the Orion molecular cloud, we detect the dynamical status of selected cores. We observationally distinguished a collapsing core in a massive star forming region from a hydrostatical one. Our approach would help significantly improve our understanding of the interaction between gravity and turbulence within molecular cloud cores in the process of star formation.

Key words: stars: formation — ISM: molecules — ISM: kinematics and dynamics — turbulence

1 INTRODUCTION

The dynamical evolution of a prestellar core is controlled by the interplay of turbulence, magnetic fields and gravity in the core, which is crucial for understanding the early phase of star formation (Mac Low & Klessen 2004; Stahler & Palla 2005; McKee & Ostriker 2007). The initiation of the gravitational collapse of a prestellar core is of particular interest, as it marks the transition toward a protostellar core (Chandrasekhar 1951; Ward-Thompson 2002; Jouni et al. 2014; Kritsuk et al. 2013; Gao et al. 2015). An important question is then how to observationally diagnose whether a prestellar core is collapsing or not. The dynamical status of a core may be identified based on theoretical predictions for the density and velocity structures (Shu 1977; Foster & Chevalier 1993; Ward-Thompson et al. 1999). Theoretical models make different predictions for the radial density profiles at different evolution stages of prestellar cores, and thus observations of the column density profile provide a tool to detect the dynamical status of the cores (Alves et al. 2001; Vazquez-Semadeni & Garcia 2001). This has motivated extensive observational studies of the column density, using far-infrared and submillimeter imaging, as well as dust extinction maps (Evans et al. 2001; Langer & Willacy 2001). However, due to the projection effect and the resolution limit, the observed column density profile can hardly distinguish different theoretical models unambiguously, except for a few special cases, where the Bonnor-Ebert type density profiles were observed through dust extinctions (Alves et al. 2001).

The gravitational collapse of a dense molecular cloud core may also be detected using the velocity structures revealed by molecular lines. For example, the presence of a gravitational collapse velocity would cause the asymmetry of optically thick lines, leading to 'blue profiles' (Zhou et al. 1993; Zhang et al. 1998; Evans 2002). In this paper, we develop a new method to identify the dynamical status of a prestellar core utilizing the radial distribution of the line width of optically thin molecular tracers. The width of molecular lines has contributions from both turbulent motions (Larson 1981; Myers 1983) and the gravitational infall velocity if it exists. We will demonstrate that the contributions from turbulence and the gravitational collapse to the line width are expected to have distinct spatial behaviors. In particular, gravitational infall motion would give rise to a rapid increase of line width toward the core center, whereas the contribution from turbulence remains almost invariant with decreasing radius. Therefore, the observed spatial distribution of line profiles may be examined to determine the relative importance of turbulence and gravitational infall. Observations toward isolated cores using single dish radio telescopes have already measured the spatial distributions of line profiles (e.g. Tafalla et al. 2004; Kirk et al. 2009). The typically larger distances of massive star forming regions and more complex nature of dense gas require even higher spatial resolution and greater sensitivity, which have been achieved by ALMA. We will define a collapsing index (CI) to characterize the dynamical status of two Orion Molecular Cloud (OMC) cores. By selecting cores with approximately spherical symmetry and simple environments, it is possible to distinguish the gravitational infall motion from turbulence, providing a new tool to measure the dynamical status of the cores.

2 THEORETICAL EXPECTATION

For a non-collapsing prestellar core, only turbulent and thermal motions contribute to the molecular line width. The contribution of turbulence to the width of an optically thin line is essentially the velocity dispersion over the length along the line of sight across the core (see the upper panel of Fig. 1). To estimate the turbulent velocity dispersion, we apply the Kolmogorov scaling law (Kolmogorov 1941) for inertial-range scales,

$$u_{\rm t}(l) \propto (\bar{\epsilon} l)^{1/3}, \tag{1}$$

where $u_{\rm t}(l)$ is the amplitude of the velocity dispersion across a separation of l, and $\bar{\epsilon}$ is the average dissipation rate of turbulent kinetic energy. Although originally developed for incompressible turbulence, the Kolmogorov scaling also applies to subsonic or transonic turbulent flows (Padoan et al. 2004), which are more commonly seen in cloud cores. Also implicitly assumed in the Kolmogorov scaling is statistical homogeneity and isotropy, which reasonably applies to a non-collapsing core (Kritsuk et al. 2013). Applying Equation (1) to the line of sight with impact parameter b toward a core of radius R (cf. Fig. 1), we find that the velocity dispersion σ_t^2 due to turbulence is given by,

$$\sigma_{\rm t}^2(b) = \frac{3}{11} u_{\rm t}^2(R) \left(\frac{2\sqrt{R^2 - b^2}}{R} \right)^{\frac{2}{3}}, \tag{2}$$

where $u_{\rm t}(R)$ is the total amplitude of the turbulent velocity fluctuations at the core radius R, and the factor $\frac{3}{11}$ accounts for the fraction of velocity fluctuations along the longitudinal direction, i.e., along the line of sight. A detailed derivation of the above equation can be found in Appendix A. Equation (2) gives the expected contribution of turbulent motions to the line width as a function of the impact parameter b, which is shown as the dotted line in the lower panel of Figure 1. We find that if turbulent motions are supersonic, e.g., in a high mass star forming core, the velocity dispersion profile has a very similar trend to this case with subsonic turbulence. Therefore, the subsequent discussions based on subsonic turbulence would also qualitatively apply to the cores with supersonic turbulence.

If a core is undergoing gravitational collapse, both the infall motion and turbulence contribute to the observed line width. To estimate the contribution of the collapse, we adopt the singular isothermal sphere (SIS) model of Shu (1977), for the collapse velocity,

$$v_{\rm g}(r) = v_{\rm g}(R) \left(\frac{r}{R} \right)^{-\frac{1}{2}}, \tag{3}$$

which is essentially the free-fall velocity due to the central singular point mass. A power law radial density profile $\rho \propto r^{-\frac{3}{2}}$ is predicted in this model, and an exact calculation of the contribution of the collapse velocity to the line width needs to account for the density variations in the core. However, for the first order approximation, we neglect the effect of the density profile on the line width. Integrating the square of the longitudinal component of the gravitational infall velocity (Eq. (3)) along the line of sight gives a velocity dispersion, $\sigma_{\rm g}^2$,

$$\sigma_{\rm g}^2(b) = v_{\rm g}^2(R) \left(\frac{R}{\sqrt{R^2 - b^2}} \ln \frac{R + \sqrt{R^2 - b^2}}{b} - 1 \right). \tag{4}$$

As $b \to 0$, $\sigma_{\rm g}^2$ approaches infinity due to the singularity of the infall velocity in the self-similar collapse model. For optically thin molecular lines, the equation predicts the line width from the collapse velocity as a function of the impact

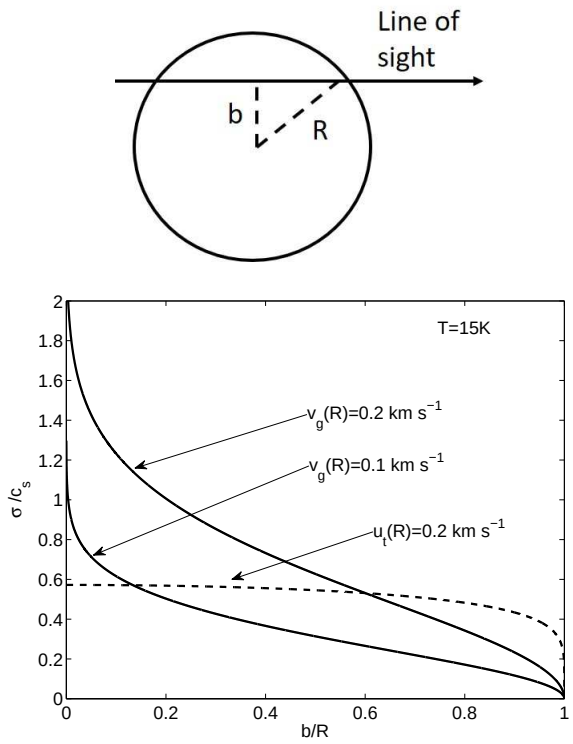

Fig. 1 *Upper*: line of sight with the impact parameter b toward a cloud core of radius R. *Lower*: theoretical expectation for the velocity dispersion (normalized to the speed of sound at 15 K by assuming the interstellar medium (ISM) mean molecular weight being 2.33 a.m.u.) as a function of the impact parameter. The *solid* and *dashed lines* represent the contributions from gravitational infall in collapsing cores and turbulent velocity dispersion in non-collapsing cores, respectively.

parameter, b. As shown in Appendix A, Equation (4) well captures the behavior of the contribution of the infall velocity to the line width of a collapsing prestellar core, even though it ignores the density variations in the core.

Turbulence also contributes to the line width of a collapsing core. From a simple dimensional analysis based on the turbulent energy source by the collapse velocity of the core (Robertson & Goldreich 2012) and the similarity theory of Kolmogorov for turbulence, we speculate that the collapse-induced turbulent velocity has a similar radial dependence as v_g, i.e., $u_t \sim r^{-1/2}$. This similarity may be expected from the fact that the energy source of both the collapse velocity and the turbulent velocity is the gravitational energy. Our speculation is subject to tests by future numerical simulations of turbulence in a collapsing core. Therefore, Equation (4) may be viewed as an approximate description for the radial dependence of the total velocity dispersion including the contributions from both the gravitational infall velocity and the collapse-induced turbulence.

As seen in the lower panel of Figure 1, the velocity dispersions caused by turbulence in non-collapsing cores (dashed line) and by gravitational infall in collapsing ones (solid lines) exhibit very different radial behaviors. Due to the faster infall velocity toward the center, line broadening by the gravitational collapse increases rapidly with decreasing b. In contrast, the turbulent velocity dispersion in the non-collapsing case is almost constant toward the center; it only decreases at the edge of the core, as the line of sight with smaller b samples turbulence across a larger length scale. Using the spatially resolved molecular line observations, the different trends of the velocity dispersion as a function of b in collapsing and non-collapsing cores provide a unique tool to detect the dynamical status of the core. The above analysis assumes that the molecular line is optically thin. Our calculation finds that, as long as the optical depth is smaller than 2 so that the molecular tracer may probe down to the center of the core, the expected spatial behavior of the line width remains qualitatively similar to that depicted in Figure 1.

In the "inside-out" scenario of the SIS model, a non-collapsing outer envelope coexists with a collapsing inner core. Therefore, the spatial distribution of the line width is expected to lie in between Equations (2) and (4). We will assume that the turbulence velocity in the non-collapsing envelope may be described by Equation (2) based on statistically homogeneous turbulence. Accounting for both the turbulence contribution from the envelope and the contribution of Equation (4) in the collapsing core region, the nonthermal line width can be approximately written as,

$$\sigma^2_{\rm NT}(b) = \frac{3}{11}u_{\rm t}^2(R)\left(\frac{2\sqrt{R^2-b^2}}{R}\right)^{\frac{2}{3}} + v_{\rm g}^2(R)\left(\frac{R}{\sqrt{R^2-b^2}}\ln\frac{R+\sqrt{R^2-b^2}}{b}-1\right), \quad (5)$$

where the parameters, $u_{\rm t}(R)$ and $v_{\rm g}(R)$, could be viewed as indicators for the amplitudes of turbulent and gravitational infall motions in a cloud core respectively.

3 SELECTED ORION CORES

As the closest region containing massive young stellar clusters, the OMC is one of the best laboratories to study star formation under the influence of massive proto-clusters. The filament of OMC 2/3 is a relatively quiescent massive star forming region, containing dense cores with different dynamical statuses (Li et al. 2013). Combining ALMA and Nobeyama observations, we obtained a high spatial resolution map of the N_2H^+ (J=1–0) line toward this region (Yue et al. 2020). The spatial resolution is $\sim$

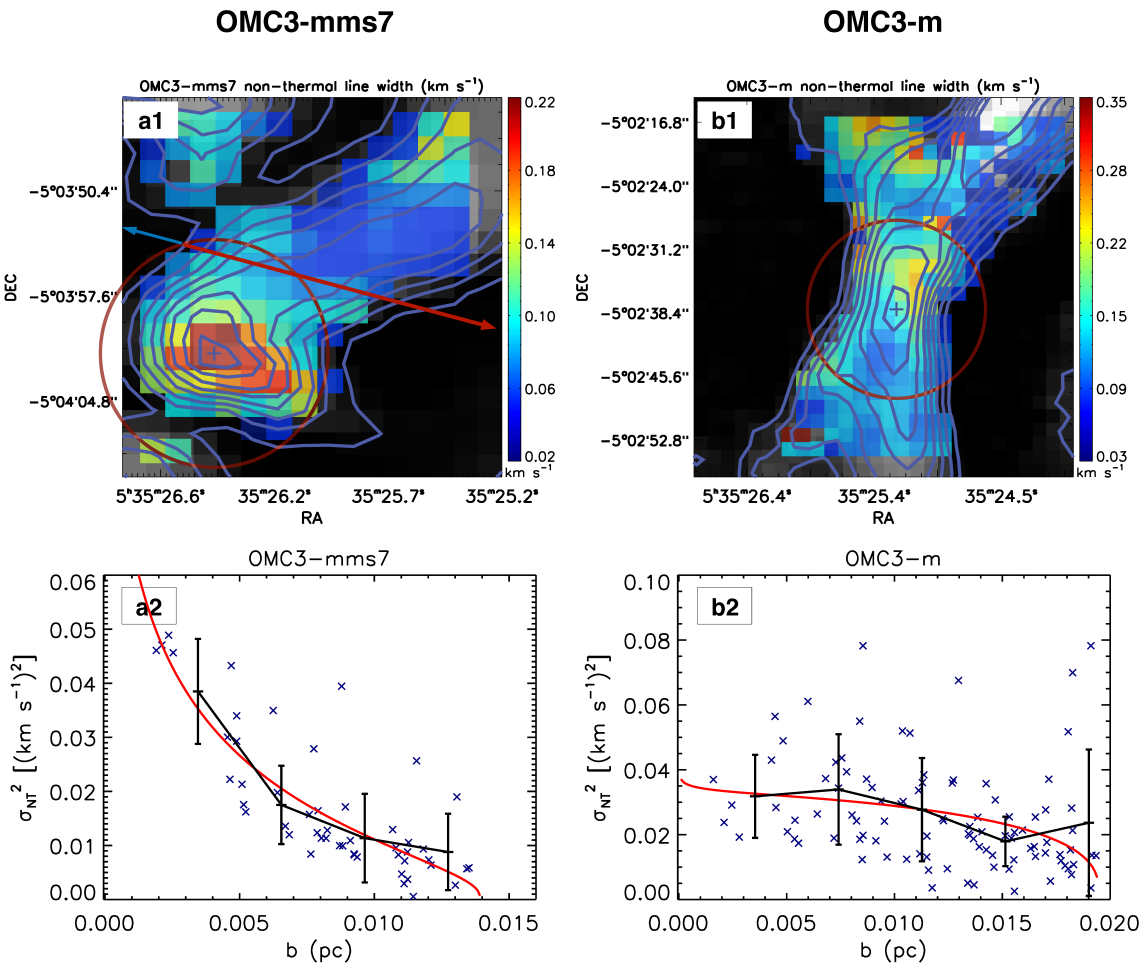

Fig. 2 Kinematics of two cores OMC3-mms7 and OMC3-m in OMC. The *contours* and the *gray background* in the upper row are the integrated intensity of N_2H^+ (J=1–0), based on which the center (*plus symbol*) and edge (*red circle*) of each core are selected. The centers of OMC3-mms7 and OMC3-m are located at R.A. = $5^h35^m26^s.4$, DEC. = $-5°4'1''.2$ and R.A. = $5^h35^m25^s.3$, DEC. = $-5°2'36''.7$, respectively. By fitting a Gaussian function to the average radial distribution of the N_2H^+ (J=1–0) intensity, the radii of OMC3-mms7 and OMC3-m are measured to be 0.014 pc and 0.020 pc, respectively (see Appendix B). The *contour lines* in a1 start at 85 mJy beam^{-1} km s^{-1} with intervals of 200 mJy beam^{-1} km s^{-1}, while the contour lines in b1 start from 100 mJy beam^{-1} km s^{-1} with intervals of 120 mJy beam^{-1} km s^{-1}. Color maps signify the non-thermal line width dispersion. In a1, the *blue* and *red arrows* indicate the direction of the outflow originating from the center position at R.A. = $5^h35^m26^s.5$, DEC.=$-5°3'55''$ (Takahashi et al. 2006, 2008). It has a *red lobe* of 0.98 pc and a *blue lobe* of 0.15 pc with a position angle of 70° from north to northeast. In the lower panels, the *blue crosses* show the non-thermal velocity dispersion from each observed pixel, while the *black lines* plot the average velocity dispersion within each radial bin. The *red curves* are the best-fit for the radial profile using Eq. (5).

$3''$, corresponding to 0.006 pc, smaller than the thermal Jeans scale $\sim$ 0.01 pc; the root mean square (rms) noise is $\sim$12 mJy beam^{-1}, and the velocity resolution is 0.11 km s^{-1}. For the cores selected for this study, our data are more than 2 times deeper compared to Hacar et al. (2018) of 25 mJy beam^{-1}, thus providing better dynamic range. The line fitting is carried out utilizing a multi-Gaussian line fitting engine, SCOUSE (Henshaw et al. 2016). In our study, we choose two dense cores, OMC3-m and OMC3-mms7, that are roughly spherical and not significantly affected by the surrounding environment. The selection of the cores and the measurement of their radii are further discussed in Appendix B.

Besides turbulence and possible gravitational motions, we also check the outflows and rotation motions which may exist in the two dense cores. There is a bipolar outflow along the east-west direction associated with OMC3-mms7; but the center of this outflow is $\sim$ $10''$ (0.02 pc) north, and on the periphery of the selected dense core (Takahashi et al. 2006). The existence of this outflow may inject energy into the core's turbulent motion, but is unlikely to cause a systematic increase

in the line width toward the center of OMC3-mms7, which we attribute to gravitational collapse. There is no outflow around OMC3-m (Takahashi et al. 2008). We also analyze the core rotation based on Xu et al. (2020) and obtain the specific angular momentums (j = J/M), i.e., 0.0005 $\mathrm{pc\ km\,s^{-1}}$ for OMC3-m and 0.003 $\mathrm{pc\ km\,s^{-1}}$ for OMC3-mms7, which correspond to less than 2% of the gravitational potential energy for each core. The relatively insignificant rotational energy found here is consistent with the majority of the literatures (e.g., Goldsmith & Arquilla 1985; Tatematsu et al. 2016). The rotational motions in these two Orion cores are negligible in supporting against gravity and should not contribute to the observed trend of line width.

The observed molecular line width is mainly contributed by thermal, turbulent and gravitational motions. Subtracting the thermal contribution ($\sigma_{\rm T}$) from the observed line width ($\sigma_{\rm obs}$), we obtain the non-thermal line dispersion $\sigma_{\rm NT}$ (Myers 1983),

$$(\sigma_{\rm NT})^2 = (\sigma_{\rm obs})^2 - (\sigma_{\rm T})^2\,, \tag{6}$$

$$\sigma_{\rm NT} = \sqrt{\frac{\Delta v^2_{\rm obs}}{8\ln(2)} - \frac{k_{\rm B}T_{\rm kin}}{m_{\rm obs}}}\,, \tag{7}$$

where $\Delta v_{\rm obs}$ is the observed full width at half maximum (FWHM) line width, $k_{\rm B}$ the Boltzmann constant, $T_{\rm kin}$ the gas kinetic temperature and $m_{\rm obs}$ the mass of the observed molecule. The kinematic information on the two selected cores is depicted in the upper panels of Figure 2. The color maps represent the non-thermal dispersions from Equation (7). The kinetic temperature, derived from JVLA NH_3 observations, varies only slightly within the cores (Li et al. 2013), and we adopt the average kinetic temperature of 15.7 K and 13.4 K for OMC3-mms7 and OMC3-m, respectively.

4 COLLAPSING INDEX

To observationally identify whether a prestellar core is collapsing, we define an empirical index, named Collapsing Index (CI), to quantify the dynamical status of the core

$$\mathrm{CI} = \frac{\sigma^2_{\rm in} - \sigma^2_{\rm out}}{\sigma^2_{\rm out}}, \tag{8}$$

where $\sigma^2_{\rm in} = \langle\sigma^2_{\rm NT-inner}\rangle$ is the average non-thermal line dispersion $\sigma^2_{\rm NT}(b)$ in the inner region with $b \le R/2$, while $\sigma_{\rm out} = \langle\sigma^2_{\rm NT-outer}\rangle$ is the average over the outer region with $b > R/2$. Based on the lower panel of Figure 1, it is expected that a core undergoing collapse would have a larger CI. Inserting Equations (2) and (4) into the definition of the index gives CI = 0.3 and 5.3, respectively. We adopt 0.3, the expected CI if only turbulence contributes to $\sigma_{\rm NT}$, as the critical value to determine whether a prestellar core is collapsing. Clearly, if the measured CI in a core is much larger than 0.3, it indicates a significant contribution from the collapse velocity to the line width.

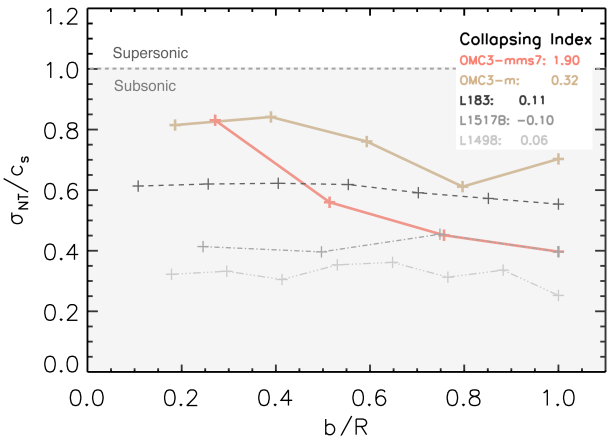

Fig. 3 The radial distribution of non-thermal velocity dispersion, normalized to the speed of sound, for five cores. The CI for each core is indicated in the legend. Both Orion cores (in *OMC3-mms7*, *OMC3-m*, *in solid lines*) and isolated cores (*L183, L1517B, L1498, in dashed and dash-dotted lines*) are in the subsonic turbulence region (i.e., non-thermal line width smaller than thermal line width). Only OMC3-mms7 has CI greater than 0.3, indicating collapse.

A calculation using the observed $\sigma_{\rm NT}$ for the selected Orion cores gives that CI = 1.90 and 0.32 for OMC3-mms7 and OMC3-m, respectively. For OMC3-mms7, we find that CI is much larger than 0.3, suggesting that gravitational collapse has already initiated in this core. On the other hand, the CI of OMC3-m is close to 0.3, indicating that its non-thermal line width is dominated by turbulence, and the core has not started to collapse. We stress that this is the first time the dynamical status of prestellar cores with radius $\le$0.02 pc has been identified. As a supportive clue on its dynamic status, the asymmetric profiles of the molecular lines ^{13}CO (J=1–0) and C^{18}O (J=1–0) in the dense core region manifest signatures of possible infall for OMC3-mms7. On the other hand, for OMC3-m, the ^{13}CO and C^{18}O lines are symmetric, likely indicating no global infall motions in it (see Appendix C).

We also examined three isolated starless cores, i.e., the high Galactic latitude core L183, and two cores in the Taurus-Auriga cloud complex, L1498 and L1517B, with different physical environments from the OMC. Due to their smaller distance ($\sim$ 150 pc) and larger size (R = 0.04 − 0.06 pc), these cores are spatially resolved by single dish telescopes. For the three cores, we make use of the observation results from Tafalla et al. 2004 to Tatematsu et al. 2017 for the spatial distribution of the N_2H^+ (J=1–0) line width; and adopt the nearly uniform kinetic temperature of 7 K, 9.4 K and 10.7 K

Table 1 Strength of Turbulent and Gravitational Motions in the Selected OMC Cores by Model Fitting

	$u_{\rm t}(R)$ [km s^{-1}]	$v_{\rm g}(R)$ [km s^{-1}]	χ^2
OMC3-mms7	0.12	0.16	0.5
OMC3-m	0.27	0.03	2.6

for L183, L1517B and L1498, respectively (Tafalla et al. 2004; Kirk et al. 2009). The CI for all these isolated starless cores is found to be smaller than 0.3, suggesting that they are not collapsing (cf. Fig. 3). It is noted that L1498 seems to display signatures of infall from its CS (J=2–1) line asymmetries (Caselli et al. 2002); and L183 is also thought to be contracting according to its possible rotation motion and spin up (Kirk et al. 2009). However, as an effective tracer of infall motion, no HCO^+ (J=1–0) asymmetry is present in L1498 or L183, indicating that they are either contracting at a very small infall speed or not collapsing at all. For L1517B, the HCO^+ (J=1–0) lines exhibit red asymmetry which indicates the existence of both envelope expansion and core collapse (EECC) motions (Tafalla et al. 2004; Fu et al. 2011). With the infall speed being small, the global EECC motion usually occurs at the very initial stage of core collapse (Gao & Lou 2010). Our CI method does not distinguish such gravitational EECC motions from turbulence.

Figure 3 displays the radial profile of the non-thermal velocity dispersion, normalized to the sound speed $c_{\rm s} \equiv \sqrt{\frac{k_{\rm B}T_{\rm kin}}{m_{\rm mol}}}$ with $m_{\rm mol}$ set to 2.33 a.m.u., for all the five cores selected in our study. Note that the non-collapsing core, OMC3-m, has a velocity dispersion larger than the three isolated cores, likely due to the more violent environment in the OMC. The velocity dispersions in all the cores are subsonic, which validates our theoretical treatment based on the scaling behavior of incompressible or weakly compressible turbulence.

The importance of the collapse velocity relative to turbulent motions can also be estimated by fitting the observed radial profile of the line width with our model, Equation (5). Applying the non-linear least-square fitting algorithm, mpfit (Markwardt 2009), we tune the two parameters, $u_{\rm t}(R)$ and $v_{\rm g}(R)$, in the equation to yield the best fits, which are represented as red lines in the bottom panels, a2 and b2 of Figure 2. The best-fit parameters are listed in Table 1. For OMC3-mms7, the gravitational collapse velocity is slightly larger than the turbulent velocity even at the edge of the core, suggesting that it is already undergoing gravitational collapse. In OMC3-m, $v_{\rm g}(R)$ is negligible, and the non-thermal velocity dispersion is dominated by turbulence, implying that the core is still in hydrostatic equilibrium.

In our analysis, the motion of rotation is not included. If rotation is considered, at least three more parameters, i.e., the scaling and radial distribution of the rotation velocity, and the inclination angle of the rotation axis have to be added in the model. The increase of complexity might smear the different features of gravity and turbulence found in this paper. The case is similar for bipolar outflows. So in the current study, we prefer to aim at the cores where rotation is not significant and bipolar outflows affect little.

The morphology of our selected cores does not deviate significantly from ideal spherical symmetry. We adopt the recipe in Li et al. (2013) and Li (2002), which derived an analytical relation between the intrinsic ellipticity and the average of its random projections. The observed axis ratios (f_{obs}) between short and long axes of the cores in our sample are 0.82 for OMC3-mms7 and 0.78 for OMC3-m, which correspond to a plausible intrinsic axis ratio (f) of 0.75 and 0.7 respectively. The resulting increase of gravitational potential energy scales with $\beta = \arcsin(\sqrt{1-f^2})/(\sqrt{1-f^2})$. The correction factor due to ellipsoid considerations are 1.09 for OMC3-mms7 and 1.11 for OMC3-m. The virial parameters (gravitational potential / kinetic energy) increase around 9% and 11%. They are not severely affected by the deviation from spherical symmetry. From the observational point of view, we consider the selected cores in this paper as spherically symmetric ones.

5 CONCLUSIONS

Based on spatially resolved line width maps of molecular cloud cores, an empirical diagnostic, named the CI, is defined to quantify the importance of the gravitational collapse velocity relative to turbulent motions. Spatially and spectrally resolved images from ALMA observations of N_2H^+ (J=1–0) lines, the best tracer to probe deep into the dense cores (Caselli et al. 2002), make it possible to evaluate the CI, allowing us to tell whether a prestellar core is undergoing gravitational collapse. Other dense core tracers such as NH_3 and H_2D^+ may also be employed in the CI analysis. In the five cores studied, we found that all isolated low mass cores have CI smaller than 0.3, indicating that they are in hydrostatical balance; while one OMC core has a CI much larger than 0.3, indicating it is collapsing. The turbulent motions in all the five cores are subsonic.

We have restricted our study to a selection of prestellar cores with spherical morphology that are not significantly affected by rotation or bipolar outflows. Our approach may be generalized to account for the effects of rotation and bipolar outflows, as well as the more complicated morphology of the cores, which, however, is out of the scope of the current study. The new approach developed in this work will help us clarify the initiation of gravitational collapse in molecular cloud cores, and is thus expected to

significantly advance our understanding of star formation in the prestellar stage.

Acknowledgements This work is supported by the National Natural Science Foundation of China (NSFC) (Grant No. 11988101 and 11911530226), and by the start-up fund from Sun Yat-Sen University. LP acknowledges financial support from NSFC (Grant No. 11973098). Dr. Tie Liu (SHAO), Dr. Lei Qian (NAOC), Dr. Zhiyuan Ren (NAOC), Dr. Zhichen Pan (NAOC) and Ms. Xuefang Xu (NAOC) are acknowledged for helpful discussions and suggestions. This paper makes use of the following ALMA data: ADS/JAO.ALMA#2013.1.00662.S. ALMA is a partnership of ESO (representing its member states), NSF (USA) and NINS (Japan), together with NRC (Canada), MOST and ASIAA (Taiwan, China), and KASI (Republic of Korea), in cooperation with the Republic of Chile. The Joint ALMA Observatory is operated by ESO, AUI/NRAO and NAOJ. We thank Dr. Shuo Kong and the CARMA-NRO Orion team for providing the ^{13}CO and C^{18}O datacubes in this region.

Appendix A: DERIVATIONS OF EQUATIONS IN SECTION 2 AND THE EFFECTS OF THE CORE DENSITY PROFILE

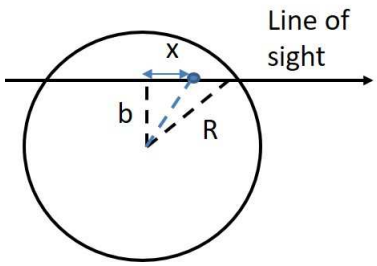

Fig. A.1 A line of sight with an impact parameter b towards a spherical core (the *circle*) with radius R. The contribution of turbulent motions to the line width along this line of sight is estimated as the turbulent velocity dispersion across the length, $2\sqrt{R^2-b^2}$, of the chord intercepted (Eq. (A.1)). The contribution to the line width due to the gravitational infall is calculated by an integration along the chord, using the velocity profile of the SIS model (Eq. (A.5) and Eq. (A.7)).

As illustrated in Figure A.1, the intersection of the line of sight with an impact parameter b with a spherical core of radius R makes a chord of length $2\sqrt{R^2-b^2}$. Applying the Kolmogorov scaling law (Eq. (1)) to this length scale, we find that the turbulent velocity dispersion $u_t^2(b)$ is,

$$u_t^2(b) = u_{\rm t}^2(R)\left(\frac{2\sqrt{R^2-b^2}}{R}\right)^{\frac{2}{3}}, \qquad \text{(A.1)}$$

with $u_{\rm t}^2(R)$ the turbulent velocity dispersion at the scale of the core radius R. The velocity dispersion is composed of the longitudinal and transverse structure functions, $u_{\rm ll}^2$ and $u_{\rm nn}^2$ respectively, by

$$u_{\rm t}^2 = u_{\rm ll}^2 + 2u_{\rm nn}^2. \qquad \text{(A.2)}$$

For incompressible or weakly compressible turbulence, we have (Landau & Lifshitz 1987)

$$u_{\rm nn}^2 = \frac{4}{3}u_{\rm ll}^2 \qquad \text{(A.3)}$$

for scales in the inertial range. The observed velocity dispersion along a line of sight with impact parameter b corresponds to the longitudinal component $u_{\rm ll}^2$ of the structure function at a separation of $2\sqrt{R^2-b^2}$ (cf. Fig. A.1). We thus have,

$$\sigma_{\rm t}^2(b) = \frac{3}{11}u_{\rm t}^2(R)\left(\frac{2\sqrt{R^2-b^2}}{R}\right)^{\frac{2}{3}}, \qquad \text{(A.4)}$$

which is Equation (2) in Section 2.

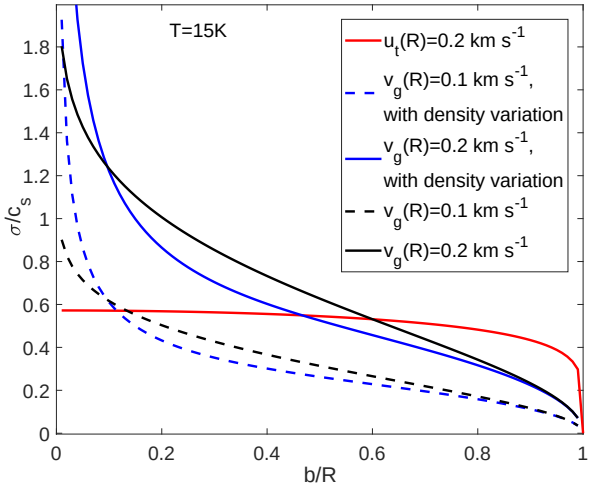

Fig. A.2 The contributions of turbulence (*red line*) and gravitational infall (*blue* and *black lines*) to the line width. The *blue* and *black lines* are based on Eq. (A.7) and Eq. (4) in the text with and without density weighting, respectively.

Based on the radial velocity profile of the SIS (Eq. (3)), we integrate the square of the longitudinal component of the collapse velocity along the intercepted chord, i.e.,

$$\sigma_{\rm g}^2(b) = \frac{1}{2\sqrt{R^2-b^2}} \times \int_{-\sqrt{R^2-b^2}}^{\sqrt{R^2-b^2}} v_{\rm g}^2(R)\left(\frac{\sqrt{b^2+x^2}}{R}\right)^{-1}\frac{x^2}{x^2+b^2}dx, \qquad \text{(A.5)}$$

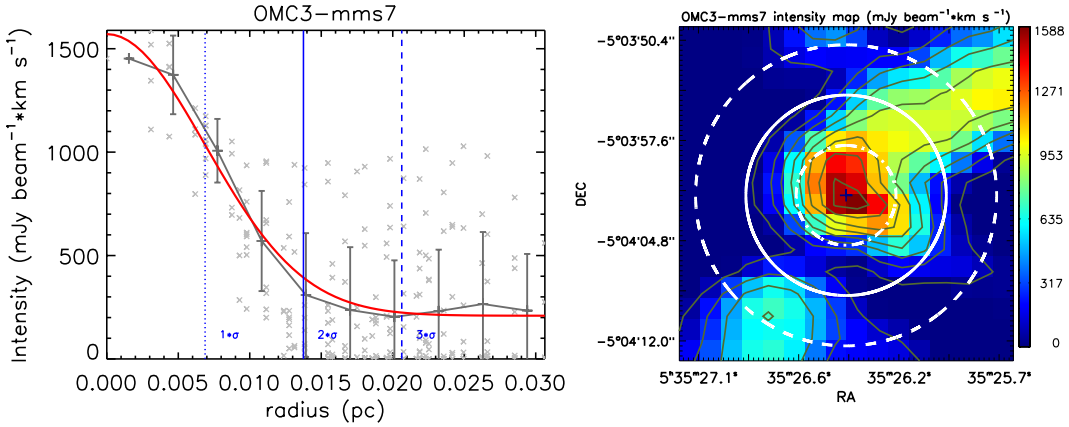

Fig. A.3 *Left*: The radial distribution of the N_2H^+ intensity for the core OMC3-mms7. The *gray dots* are the observed N_2H^+ intensity at each pixel. The *black line* is the average intensity within the bin size of ~ 0.003 pc, while the error bars indicate the rms of the intensity variations in each bin. The mean noise (rms) of the integrated map in this region is ~ 12 mJy beam^{-1} km s^{-1}. The *red line* is the Gaussian function with a standard deviation of $\sigma = \sim 0.007$ pc, which best fits the *black line*. The *blue lines* represent radii of 1, 2 and 3σ from the core center. The *blue solid line* is adopted as the core radius ($R = 0.014$ pc) in the main text. *Right*: The N_2H^+ intensity map of OMC3-mms7. The contour starts from 85 mJy beam^{-1} km s^{-1} with a step of 200 mJy beam^{-1} km s^{-1}. The *white lines* correspond to radii of 1, 2 and 3σ.

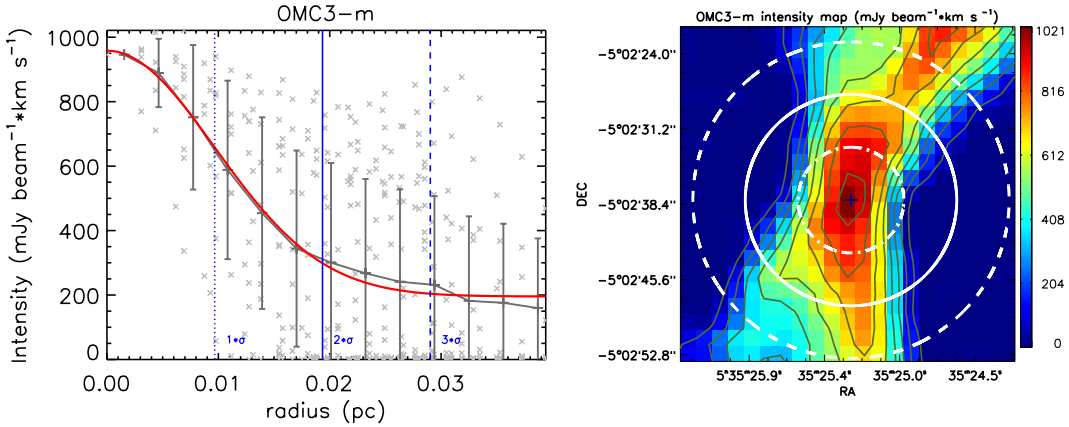

Fig. A.4 Same as Fig. A.3, but for OMC3-m. *Left*: The radial distribution of the average N_2H^+ intensity (*black line*) is fit by a Gaussian function with a standard deviation of $\sigma = \sim 0.01$ pc. The *blue lines* are located at distances of 1, 2 and 3σ from the center. The *blue solid line* is adopted as the core radius (0.02 pc) in the main text. *Right*: The N_2H^+ intensity map of OMC3-m. The contours start from 100 mJy beam^{-1} km s^{-1} with a step of 120 mJy beam^{-1} km s^{-1}. The *white lines* are locations of 1, 2 and 3σ from the core center.

where the integration variable x is illustrated in Figure A.1. The integral in the above equation can be calculated analytically, and we find that

$$\sigma_{\rm g}^2(b) = v_{\rm g}^2(R)\left(\frac{R}{\sqrt{R^2-b^2}}\ln\frac{R+\sqrt{R^2-b^2}}{b} - 1\right), \tag{A.6}$$

which is Equation (4) in the text.

An accurate estimate for the contribution of the collapse velocity to the line width needs to account for the radial density variations in the core along the line of sight. Using the radial density profile, $\rho \propto r^{-\frac{3}{2}}$, in the SIS model of Shu (1977) and applying a density weighting factor of ρ^2, the contribution to the line width by the gravitational infall is given by,

$$\sigma^2_{{\rm g}(\rho)}(b) = \frac{\int_{-\sqrt{R^2-b^2}}^{\sqrt{R^2-b^2}} v_{\rm g}^2(R)\left(\frac{\sqrt{b^2+x^2}}{R}\right)^{-1}\frac{x^2}{x^2+b^2}\left(\frac{\sqrt{b^2+x^2}}{R}\right)^{-3}dx}{\int_{-\sqrt{R^2-b^2}}^{\sqrt{R^2-b^2}}\left(\frac{\sqrt{b^2+x^2}}{R}\right)^{-3}dx}. \tag{A.7}$$

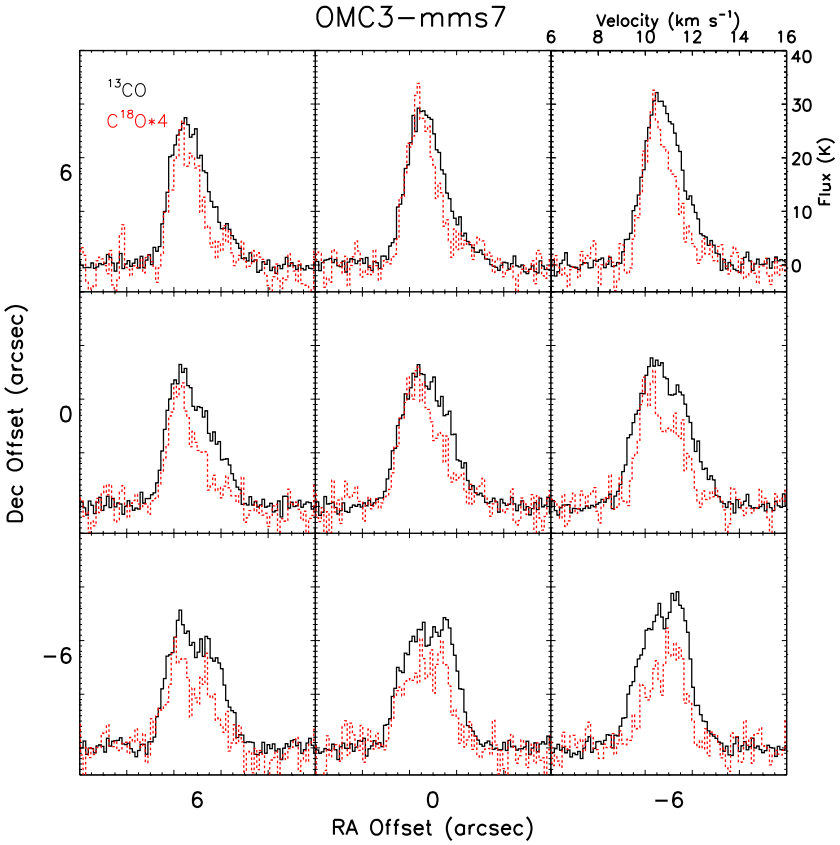

Fig. A.5 The ^{13}CO J = 1–0 (*black solid lines*) and C^{18}O J = 1–0 (*red dashed lines*) molecular line map in the OMC3-mms7 core. The spectra are taken from the CARMA-NRO Orion Survey with a resolution of around $8''$ (Kong et al. 2018). The whole map is centered around OMC3-mms7 (R.A. = $5^h35^m26^s.4$, DEC. = $-5°4'1''.2$) with a grid spacing of $6''$, and covers a region size of $18'' \times 18''$. The radius of OMC3-mms7 is $7.2''$ (0.014 pc).

The numerator in this equation cannot be integrated analytically. The numerical evaluation of the density weighted velocity dispersion (Eq. (A.7)) by the gravitational collapse is shown as the blue curves in Figure A.2. The black curves display the prediction of Equation (4) in the text, which ignores the density variations in the core. As seen in Figure A.2, the behaviors of the blue and black lines with and without density weighting are qualitatively very similar, suggesting that, as a first order approximation, Equation (4) in the text well captures the key features of the contribution of the infall to the line width of a collapsing prestellar core.

Appendix B: MEASUREMENT OF THE CORE RADIUS

In our study, we selected two starless Orion cores based on the integrated intensity of N_2H^+ emission lines. To avoid complexities, the two selected Orion cores are relatively isolated and have approximately spherical morphology. The high-resolution observational data allow a study of the radial profile of the molecular emission lines. We treat the selected cores as spherically symmetric objects and identify the position where the molecular line emission peaks as the center. We find that the intensity of the emission line as a function of the distance to the core center may be fit by a Gaussian function (see the red lines in Figs. A.3 and A.4). In the text, we take the core radius, R, to be 2σ, where σ is the standard deviation of the best fit Gaussian function. With this method, we find that R =0.014 pc for OMC3-mms7 and 0.020 pc for OMC3-m. The choice of $R = 2\sigma$ is based on the consideration that it includes sufficient information inside the core, but excludes the surrounding gas along the filament around the core. To examine whether the choice of the core radius affects our conclusion, here we calculate the CIs with R set to 1σ and 3σ. The resulting CI values are listed in Table B.1, which confirms that, for both OMC3-mms7 and OMC3-m, the different choices for the core radius change the CI only slightly. This suggests that the determination

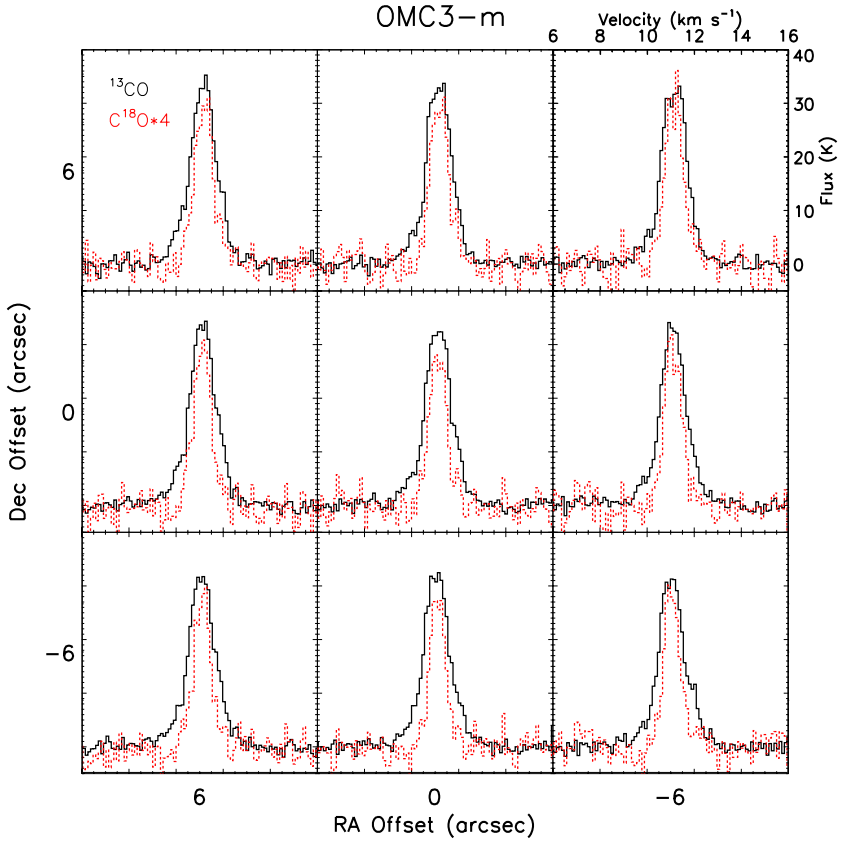

Fig. A.6 Maps of the ^{13}CO J = 1–0 (*black solid lines*) and C^{18}O J = 1–0 (*red dashed lines*) molecular lines in the OMC3-m core. The whole map is centered around OMC3-m (R.A. = $5^h35^m25^s.3$, DEC. = $-5°2'36''.7$) with a grid spacing of $6''$, and covers a region size of $18'' \times 18''$. The radius of OMC3-m is $10''$ (0.02 pc).

Table B.1 CI when Choosing Different Core Radii

	CI ($R = 1\sigma$)	CI ($R = 2\sigma$)*	CI ($R = 3\sigma$)
OMC3-mms7	1.26	1.90	1.39
OMC3-m	0.06	0.32	0.39

Here σ is the standard deviation of the best fit Gaussian function to the intensity map. For OMC3-mms7, σ is 0.007 pc and for OMC3-m, σ is 0.01 pc. * These radii are used in the main text.

of the cores' dynamic status by the CI is insensitive to the choice of the core radius. Therefore, our conclusion concerning the dynamic status of the cores selected in this study appears to be robust.

Appendix C: THE ^{13}CO AND C^{18}O LINE PROFILES OF OMC3-MMS7 AND OMC3-M

In Figure A.5 and Figure A.6, we plot the ^{13}CO (J = 1–0) and C^{18}O (J = 1–0) line profiles in OMC3-mms7 and OMC3-m, respectively. The datacubes are taken from the CARMA-NRO Orion Survey (Kong et al. 2018). The observations were carried out by the Combined Array of Research in Millimeter-wave Astronomy (CARMA) between 2013 and 2015. Combined with the single-dish data from the Nobeyama telescope, this survey provides a map of the Orion A cloud with high spatial resolution and high dynamical range. The beam sizes are $8'' \times 6''$ for the observation of ^{13}CO and $10'' \times 8''$ for C^{18}O. The rms noises of ^{13}CO and C^{18}O maps are 0.64 K and 0.47 K per channel, respectively. They have the same velocity resolution of 0.22 km s^{-1}. For OMC3-m (Fig. A.6), the lines are rather symmetric, indicating no significant infall motion. On the other hand, the lines in OMC3-mms7 (Fig. A.5) appear to be asymmetric, and the stronger blue-shifted shoulders likely represent signatures of infall. These are consistent with our conclusion in the text, supporting the validity of our new approach to detect the dynamical status of prestellar cores based on the CI measurement.

References

Alves, J., Lada, C. J. & Lada, E. A. 2001, Nature, 406, 159
Caselli, P., Benson, P. J., Myers, P. C. & Tafalla, M. 2002, ApJ, 572, 238

Chandrasekhar, S. 1951, P. Roy. Soc. Lond. A Mat., 210, 26
Evans, N. J., II, Rawlings, J. M. C., Shirley, Y. L., & Mundy, L. G. 2001, ApJ, 557, 193
Evans, N. J., II. 2003, in Curry C. L., Fich M., eds, Proc. Conf., Chemistry as a Diagnostic of Star Formation (Canada, Ottawa: NRC Research Press) 157
Foster, P. N., & Chevalier, R. A. 1993, ApJ, 416, 303
Fu, T., Gao, Y. & Lou, Y.-Q. 2011, ApJ, 741, 113
Gao, Y., & Lou, Y.-Q. 2010, MNRAS, 403, 1919
Gao, Y., Xu, H., & Law, C. K. 2015, ApJ, 799, 227
Goldsmith, P. F., & Arquilla, R. 1985, Protostars and Planets II, 137
Hacar, A., Tafalla, M., Forbrich, J., et al. 2018, A&A, 610, A77
Henshaw, J. D., Longmore, S. N., Kruijssen, J. M. D., et al. 2016, Astrophysics Source Code Library (ASCL), record ascl: 1601.003
Jouni, K., Federrath, F., & Henning, T. 2014, Science, 344, 183
Kirk, J. M., Crutcher, M., & Ward-Thompson, D. 2009, ApJ, 701, 1044
Kolmogorov, A. N. 1941, DoSSR, 30, 301
Kong, S., Arce, H. G., Feddersen, J. R., et al. 2018, ApJS, 236, 25
Kritsuk, A. G., Lee, C. T., & Norman L. M. 2013, MNRAS, 436, 3247
Landau, L. D., & Lifshitz, E. M. 1987, Fluid Mechanics (2nd eds.), (Elsevier: New York)
Langer, W. D., & Willacy, K. 2001, ApJ, 557, 714
Larson, R. B. 1981, MNRAS, 194, 809
Li, D. 2002, Ph.D. Thesis, *https://ui.adsabs.harvard.edu/abs/2002PhDT.....10L/abstract*
Li, D., Kauffmann, J., Zhang, Q., & Chen, W. 2013, ApJL, 768, L5
Mac Low, M.-M., & Klessen, R. S. 2004, Rev. Mod. Phys., 76, 125
McKee, C. F., & Ostriker, E. C. 2007, ARA&A, 45, 565
Markwardt C. B. 2009, in Bohlender D. A., Durand D., Dowler P., eds, Astronomical Society of the Pacific Conference Series 411, Astronomical Data Analysis Software and Systems XVIII, 251 (arXiv:0902.2850)
Myers, P. C. 1983, ApJ, 270, 105
Padoan, P., Jimenez, R., Nordlund, Å., & Boldyrev, S. 2004, Phys. Rev. Lett., 92, 191102
Robertson, B., & Goldreich, P. 2012, ApJ, 750, 31
Stahler, S. W., & Palla, F. 2005, The Formation of Stars
Shu, F. H. 1977, ApJ, 214, 488
Tafalla, M., Myers, P. C., Caselli, P., & Walmsley, C. M. 2004, A&A, 416, 191
Takahashi, S., Saito, M., Takakuwa, S., et al. 2006, ApJ, 651, 933
Takahashi, S., Saito, M., Ohashi, N., et al. 2008, ApJ, 688, 344
Tatematsu, K., Liu, T., Ohashi, S., et al. 2017, ApJS, 228, 12
Tatematsu, K., Ohashi, S., Sanhueza, P., et al. 2016, PASJ, 68, 24
Vazquez-Semadeni, E., & Garcia, N. 2001, ApJ, 557, 727
Ward-Thompson, D., Motte, F., André, P. 1999, MNRAS, 305, 143
Ward-Thompson, D. 2002, *Science*, 295, 76
Xu, X., Li, D., Dai, Y. S., et al. 2020, ApJ, 894, L20
Yue, N., Li, D., Zhang, Q., et al. 2020, accepted by RAA, arXiv:2006.04168
Zhang, Q., Ho, P. T. P., & Ohashi, N. 1998, ApJ, 494, 636
Zhou, S., Evans, N. J. II., Kompe, C., & Walmsley, C. M. 1993, ApJ, 404, 232